IOP Publishing
Plasma Sources Science and Technology
Plasma Sources Sci. Technol. **32** (2023) 064002 (10pp)
https://doi.org/10.1088/1361-6595/acdbe7

Experimental and numerical investigation of surface streamers in a nanosecond pulsed packed bed reactor

Mengbo Li[1], She Chen[1,*], Yifei Zhu[2,*], Yunjie Li[1], Feng Wang[1], Yingzhe Cui[3] and Chijie Zhuang[3]

[1] College of Electrical and Information Engineering, Hunan University, Changsha 410082, People's Republic of China
[2] School of Electrical Engineering, Xi'an Jiaotong University, Xi'an 710049, People's Republic of China
[3] The State Key Laboratory of Power Systems, Department of Electrical Engineering, Tsinghua University, Beijing 100084, People's Republic of China

E-mail: chenshe@hnu.edu.cn and yifei.zhu.plasma@gmail.com

Received 30 November 2022, revised 21 May 2023
Accepted for publication 6 June 2023
Published 19 June 2023

Abstract
Packed bed reactor (PBR) is the commonly used configuration in plasma catalysis, and its plasma characteristics have been extensively investigated. The filled catalysts in PBR make it challenging to carry out *in-situ* measurements of electric fields, and limited experimental data have been obtained. We investigated the surface streamer propagation and electric field distribution in a simplified PBR through simulations and experiments. The simplified PBR in the experiments is comprised of a blade-plate electrode structure filled with an Al_2O_3 column ($\varepsilon_r = 9$) in the discharge gap. An ICCD camera and an electric field diagnosis method called EFISH (electric field induced second harmonic generation) were employed, and a two-dimensional fluid model was established for the simulation. Four discharge types in the PBR were identified based on ICCD images and simulation results, including polar discharge at the contact areas, surface streamer along the dielectric column, expansion of surface discharge along the dielectric column, and surface ionization waves along the dielectric plate. Surface streamers with opposite propagation directions were found in the model, namely the forward streamer during the pulse rising time and the reverse streamer during the pulse falling time. Notably, the reverse streamer exhibits a significantly lower velocity compared to the forward streamer. Both experimental measurements and simulation were conducted to investigate the spatiotemporal electric field near the surface of the packing material. The results of both E_{exp} and E_{sim} showed peaks with opposite polarities, and exhibited similar trends. In the simulation, the forward streamer head showed a higher electric field compared to the reverse streamer head. Moreover, during the rest pulse time, the surface electric field was more intense at the contact areas than in other regions. The findings of this work provide valuable insights into the discharge mechanism and electric field on the catalytic material surface within the PBR.

* Authors to whom any correspondence should be addressed.

 © 2023 IOP Publishing Ltd

Supplementary material for this article is available online

Keywords: plasma-catalysis, packed bed reactor, simulation, EFISH, surface streamer

(Some figures may appear in colour only in the online journal)

1. Introduction

Plasma-catalysis, due to the combination of plasmas and chemical catalysts, exhibits strong chemical selectivity and high efficiency in specific chemical reactions, which is gaining recognition as an alternative method in research fields like volatile organic compounds (VOCs) removal [1–2], combustion [3] and energy conversion [4]. A common coupling method involves filling the catalyst directly into the dielectric barrier discharge (DBD) reactor, referred to as the packed bed discharge reactor (PBR) [5].

Both plasma and catalysis interact with each other in PBR, with plasma affecting the physicochemical properties of the catalyst [6, 7] and catalyst influencing plasma discharge modes and parameters [8–10]. Several studies have investigated the dynamic discharge evolution in PBR [11–18]. The presence of surface streamers on the catalyst surface has been observed in different PBR structures. Surface streamers play an essential role in the plasma catalysis interaction. The coupling mechanism of plasmas and chemical catalysts is very complex, which can be better understood by investigating the properties of plasma and catalytic materials in plasma-catalysis. However, due to the presence of the catalyst in the discharge, some *in-situ* measurements are too challenging to perform. Numerical simulations have thus become an effective tool for such studies [19–21]. For instance, Wang *et al* built a two-dimensional fluid model to investigate the propagation of the streamer in a PBR operating in dry air, and their simulation results demonstrated the influence of different packing materials on the PBR performance [22]. Van Laer and Bogaerts employed a fluid model to study a packed bed DBD and predict the influence of the packing materials and gap sizes on the plasma characteristics [23]. Xiong *et al* investigated the initiation and propagation of the surface streamer in the PBR. However, limitations in PBR models remain [24], including whether the simulation data accurately reflect the actual experimental results. Additionally, a majority of the literature lacks a thorough comparison between simulations and experiments.

The electric field is one of the critical parameters in plasma catalysis that affects electron mobility, average electron energy, and other parameters. It also plays a critical role in determining discharge development and influencing chemical reactions [25]. Although the measurement of the electric field will help reveal the coupling mechanism, the experimental data on the electric field in PBR is limited. With the advancements in diagnostic technology, electric field induced second harmonic generation (EFISH), as an *in-situ* electric field measurement method, has been implemented in the plasma electric field diagnosis in recent years because of its wide adaptability to various gases and high spatiotemporal resolution [26, 27]. EFISH is a special four-wave mixing process that arises from the interaction between the laser and the applied electric field. Researchers have successfully applied EFISH to investigate the electric field distribution in various plasma systems, such as the plasma jet [28], DC corona discharge [29], DBD [30], and surface DBD [31]. Chng *et al* performed a theoretical and experimental study by using focused Gaussian beams and examined the consequent effects on the EFISH signal [32]. Nakamura *et al* developed a method to calibrate and obtain the electric field profile along a probing optical path [33]. This method is suitable for restoring the electric-field profile containing a single peak, which is the electrostatic field. Meanwhile, the validity of restoring the electric field in streamer discharges should be carefully discussed. The key to implementing EFISH is the complete laser optical path in the measurement area. Nonetheless, the random distribution of catalytic materials in PBR obstructs the optical path of the laser measurement system. To acquire the electric field distribution in PBR through EFISH, the PBR employed in our EFISH measurement needs simplification.

In this study, the plasma parameters and electric field distribution of a PBR are investigated through experiments and numerical simulations. Section 2 presents the descriptions of the experimental setup and model. In section 3, the electric field distribution and discharge images of the PBR obtained from experiments and the simulation results are discussed. Finally, the conclusions are presented in section 4.

2. Description of the experiment and model

2.1. The structure of simplified PBR

As previously mentioned, the random distribution of packing material in PBR obstructs the optical path, posing a challenge for obtaining electric fields through EFISH. The catalyst surface is a critical position for the reactions between the plasma and catalyst, and the surface streamer plays a significant role in facilitating these coupling reactions. In this work, we focused on the surface streamer and used a simplified PBR configuration, as illustrated in figure 1(a), which includes front and side views of the PBR (figures 1(a)(i) and (ii)). Blade-plate electrodes were used in our experiments. The brass blade with a length of 30 mm and a curvature radius of 0.2 mm was connected to the homemade nanosecond pulse (pulse rise time: 500 ns; FWHM: 500 ns). The 1 mm-thick Al_2O_3 dielectric plate with a size of 50 mm × 50 mm was attached to the ground electrode. The pulse voltage was monitored using a voltage probe (Tektronix P6015), while a current probe

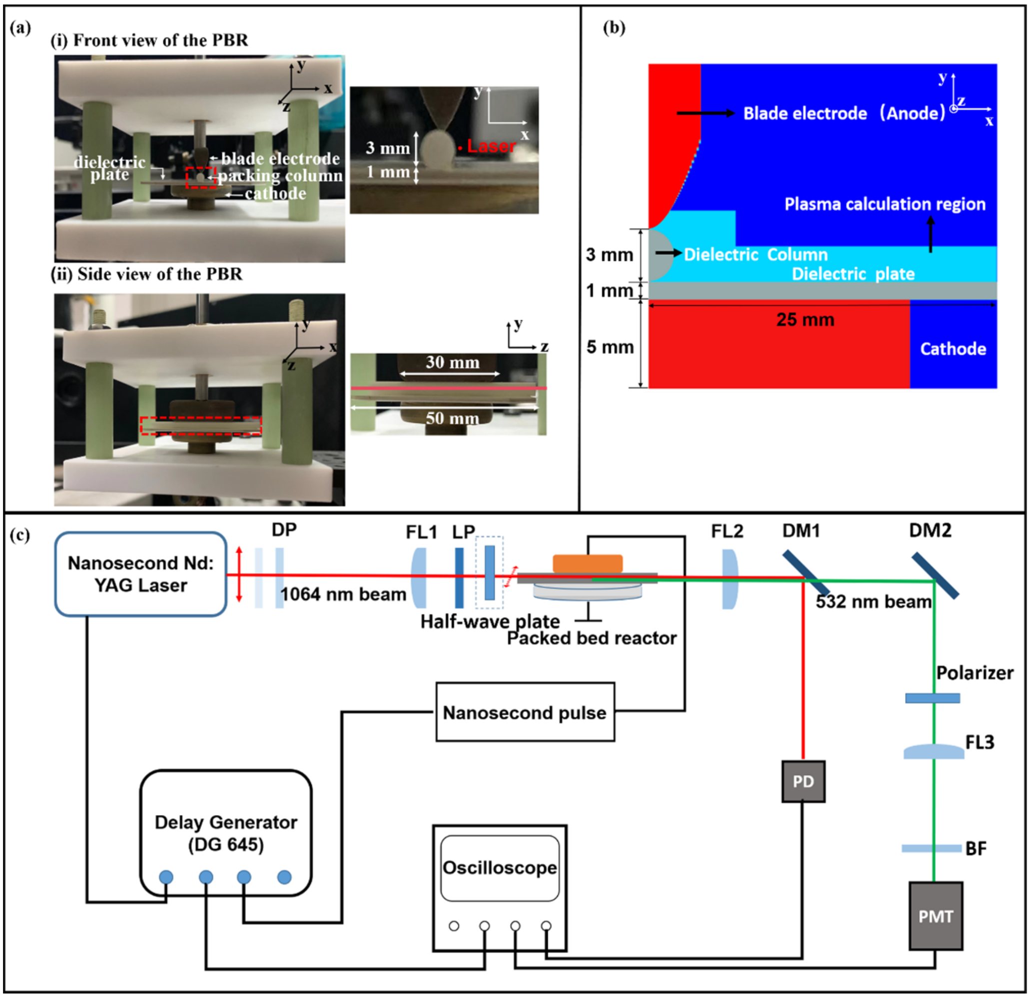

Figure 1. (a) The configuration of the simplified PBR used in the EFISH experiment. (b) The structure of two-dimensional symmetry simplified PBR model. (c) Experimental configuration of EFISH. DP: dispersion prism; LP: long pass filter; Half-wave plate; FL1, FL2 and FL3 are plano-convex lenses with focal lengths of 500 mm, 150 mm, and 250 mm, respectively; DM1: dichroic mirror (1064 nm reflecting, 532 nm transmitting); DM2: dichroic mirror (532 nm reflecting, 1064 nm transmitting); PD: photodiode; PMT: photomultiplier tube; Polarizer; BF: 532 nm bandpass filter.

(Pearson Electronics) was connected to the ground electrodes. A column made of Al_2O_3 material with a length of 50 mm and a diameter of 3 mm was utilized as the packing material to facilitate EFISH conversion. The discharge gap between the electrodes was set at 3 mm.

2.2. Model description

The simulation of surface streamers was performed in a two-dimensional symmetric PBR using the PASSKEy (Parallel Streamer Solver with KinEtics) code [34], which has previously been applied to simulate surface DBD [35], streamer discharge [36], and plasma jet [37]. The simulation method incorporates continuity equations with the drift-diffusion approximation and the energy conservation equation for the mean electron energy, while Poisson's equation is utilized to solve for the electric field. Further details regarding the algorithms can be found in [38] and [39].

The simulation model employs a cross-sectional geometry of the PBR that resembles the structure of the front view of the PBR, as shown in figure 1(a)(i). In order to reduce the computation load, we utilized only half of the cross-sectional area in our simulation. The dimensions of the simulation geometry are illustrated in figure 1(b). The thickness of the two-dimensional symmetric model, which represents the length in the z-axis direction. In our model, we have set a thickness of 30 mm, which is consistent with the length of the blade electrode in the experiment. The positive pulse voltage obtained from the experiments is smoothed and applied to the blade electrode. The discharge gap distance was 3 mm and filled with a single Al_2O_3 column ($\varepsilon_r = 9$). Our simulation approach aimed to closely approximate the actual PBR size in our experiment. Photoionization was included in the model by solving the Helmholtz differential equations in the model. Moreover, a plasma seed with a diameter of 0.15 mm and peak density of 10^{18} m^{-3} was placed at the tip of the blade electrode to ensure the initiation of the surface steamer from the anode. To avoid overly dense mesh, the contact points were enlarged and rounded. A uniform mesh size of 1 μm is utilized within the plasma domain, covering the region of 0 mm $< x <$ 20 mm and 0 mm $< y <$ 9.5 mm. Outside this region, the mesh size increases exponentially. The chemistry considered in the model for dry air ($N_2/O_2 = 78/21$) involved 14 species and 38 reactions, with an initial temperature of 300 K and a gas pressure of 1 atm. Detailed information regarding the species and reactions used in our calculation can be found in [38] and the supplementary file.

2.2.1. Experimental setups. The EFISH experimental setup is depicted in figure 1(c), which is similar to the one used in [29]. An Nd: YAG laser generates a vertical polarized 1064 nm fundamental laser with a pulse duration of 5 ns. The laser pulse energy fluctuation is less than 2%. The fundamental laser is focused at the measurement area by an f = 500 mm plano-convex lens (FL1). A dispersion prism (DP) is placed inside Nd:YAG laser to eliminate 532 nm stray light from the laser equipment. A long-pass (LP) filter is positioned before the measurement area to remove stray 532 nm light generated from the optics lens. In this study, we measured different electric field components within the PBR. Notably, the laser beam is polarized parallel to the applied field component to enhance the signal-to-noise ratio during the measurement of different electric field components. Consequently, a half-wave plate is positioned before the measurement area when measuring the horizontal electric field.

Due to the applied electric field, second harmonic light (532 nm) is generated and recollimated by an f = 150 mm plano-convex lens (FL2). The two beams are separated by a dichroic mirror (DM1) that reflects the fundamental laser into a PIN photodiode (PD). The second harmonic signal is focused by an f = 250 mm plano-convex lens (FL3) and is then incident into a monochromator equipped with a PMT (Hamamatsu photomultiplier). A polarizer is positioned before the FL3 to separate the vertically and horizontally polarized second harmonic signals. A 532 nm bandpass filter is placed before the PMT to remove the stray light. The signals are recorded by an oscilloscope (LECROY). The radius of the laser beam at the focal point is estimated to be 100 μm, and the confocal parameter is about 3 cm. The relationship between the intensity of the second harmonic signal and the applied electric field is represented in equation (1)

$$I_{\mathrm{SH}}^{(2\omega)} \sim \frac{\pi^2 [\chi^{(3)}_{i,j,k,l} N P_0^{(\omega)}]^2}{(\lambda^{(\omega)})^2 z_R^2} \left| \int_{-L}^{L} E_{\mathrm{ext}}(z) \cdot \frac{\exp(i \cdot \Delta k z)}{1 + i(\frac{z}{z_R})} \mathrm{d}z \right|^2 . \quad (1)$$

Here, ω is the fundamental laser frequency. $\lambda^{(\omega)}$ is the wavelength at the fundamental frequency. E_{ext} is the applied electric field. N is the gas molecular density. $\chi^{(3)}_{i,j,k,l}$ is the third-order nonlinear susceptibility tensor. 2 l is the interaction length between the laser and the applied electric field. Δk is the wavevector mismatch between the fundamental laser and the second harmonic. $P_0^{(\omega)}$ is the power carried by the fundamental laser (equation (2)). $E_0^{(\omega)}$ is the amplitude of the electric field of the laser. z_R is the Rayleigh range of the beam, which is related to the beam waist $w_0^{(\omega)}$ (equation (3))

$$P_0^{(\omega)} \propto \left[w_0^{(\omega)}\right]^2 \cdot \left|E_0^{(\omega)}\right|^2 \quad (2)$$

$$z_R = \frac{\pi \left[w_0^{(\omega)}\right]^2}{\lambda^{(\omega)}}. \quad (3)$$

To facilitate the conversion of the second harmonic signal (SHG) into an electric field, a cylindrical catalyst was used as the packing material between the discharge gap instead of the catalytic bead. The SHG relates to the interaction length between the electric field and the laser. In contrast to the catalytic bead, the electric field length at various positions within the PBR containing a cylindrical catalyst remained consistent, approximately 30 mm of the blade length. Despite the occurrence of filamentary surface discharges along the column, it is noteworthy that the electric field measurements in this study represent an average field along the cylindrical axis. These measurements still provide valuable insights into the discharge mechanism within the PBR.

3. Results and discussion

3.1. The electrical parameters and discharge evolution in PBR

Figure 2 illustrates the voltage and current waveforms obtained from both experiments and simulations. The applied voltage V_{exp} peaks at roughly 24 kV and has a rise time of 500 ns. The pulse repetition rate is set as 1 Hz in experiments. As for measured total current I_{exp}, it represents the average value of the currents under consecutive pulses.

We calculated the displacement current ($I_{\mathrm{dis}} = C \times \mathrm{d}V_{\mathrm{exp}}/\mathrm{d}t$) and found that it contributed little to the I_{exp} due to the modest pulse change rate. Therefore, we ignored the effect of I_{dis} on I_{exp} in this work. Regarding simulation current I_{sim}, we adopted the smoothed V_{exp} as the voltage input of the simulation. I_{sim} is the integral of the fluxes of negative and positive charge through the surface of the anode [40].

Figure 2 depicts the current peaks of I_{exp} and I_{sim} with different polarities during the rising and falling edges, indicating the occurrence of discharges at the respective pulse edges. However, due to the signal delay introduced by the measurement cable, the waveforms of I_{exp} and I_{sim} do not exhibit good time matching. During the pulse rising edge, I_{sim} increases rapidly at t = 500 ns, reaching its first current peak at t = 518 ns, followed by a dramatic drop, whereas I_{exp} reaches its first current peak at t = 625 ns. Both current development processes at this stage correspond to the development of the forward surface streamer, as shown in figures 3 and 4. The first current peak of I_{sim} (4.8 A) is significantly greater than that of I_{exp} (1.23 A). As mentioned earlier, a cross-section of the dielectric column perpendicular to the laser propagation was adopted in the model, assuming the discharge to be uniform along the cylindrical axis. However, the discharge along the cylindrical axis was filamentary in reality. Differences in the morphology of the surface streamer between the experiment and simulation

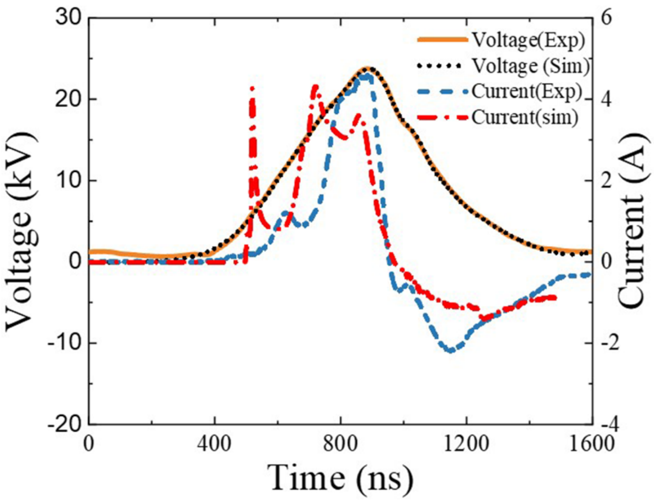

Figure 2. Waveforms of voltage and current from experiments and simulation.

result in inconsistency in the first current peak value. The pulse continues to rise, and I_{sim} and I_{exp} grow again at a rate of 0.014 A ns^{-1}, reaching another current peak before decaying to zero. During the pulse falling edge, both I_{sim} and I_{exp} grow reversely, reaching their reverse peaks and indicating reverse breakdown.

We utilized the multi-frame ICCD camera (SIM 8) to observe the discharge evolution of the PBR filled with a single Al_2O_3 column under a pulse peak of 24 kV. The synchronization was achieved by adjusting the time delay between the pulse and ICCD trigger signal. We captured the discharge development of the PBR with a frame exposure time of 5 ns, presented in figure 3. As depicted in figure 3(b), the discharge propagates along the surface of the dielectric material and can be roughly classified into a surface streamer on the dielectric column and a surface ionization wave on the dielectric plate. During the rising pulse edge, the discharge initiated at the contact areas between the anode and the dielectric column at $t_{ICCD} = 580$ ns, and then the polar discharge persisted until $t_{ICCD} = 635$ ns. With the pulse's increment, the forward surface streamer propagates from the anode to the middle part of the dielectric column during $t_{ICCD} = 635$ ns–655 ns. After the streamer head arrives at the middle part of the column, the streamer propagation velocity increase significantly, and the streamer reaches the bottom part of the column in 5 ns ($t_{ICCD} = 660$ ns). A similar phenomenon was also observed in [8]. When the streamer head arrives at the bottom part of the column, the discharge expands, and a volume discharge is visible between the bottom part of the column and the dielectric plate. The pulse continues to rise, and a surface ionization wave propagates outward along the dielectric plate surface.

The paper investigates the discharge evolution of the model by analyzing the distribution of electron and $N_2(C^3\Pi_u)$ number density on the dielectric column surface. The distribution of $N_2(C^3\Pi_u)$ is a useful way to characterize the discharge evolution [40]. In order to investigate the time-resolved particle number density on the dielectric column surface more effectively, a polar coordinate system was employed, with the centroid of the cylinder serving as the origin point. The top, middle, and bottom of the column are represented by $\theta = 90°$, $0°$, and $-90°$, respectively, as shown in figure 4.

It can be seen from figures 4 and S1 that the discharge begins at the top contact area between the anode and the column at $t_{sim} = 500$ ns. At this time, figure 4 illustrates that the maximum electron density and maximum $N_2(C^3\Pi_u)$ density are observed at the top of the column. A local discharge is visible at $t_{sim} = 504$ ns, coinciding with the occurrence of maximum electron density at the bottom of the column. As the pulse increases, a surface streamer propagates toward the cathode along the surface of the dielectric column, while the local discharge at the bottom of the column also expands. During the propagation of the forward surface streamer, the $N_2(C^3\Pi_u)$ and electron density at that location reach a maximum when the streamer head reaches a specific location. Subsequently, the $N_2(C^3\Pi_u)$ density rapidly declines as the streamer head passes. The streamer head reaches the middle part of the column at $t_{sim} = 514$ ns, and the propagation velocity of the surface streamer can be estimated at approximately 0.16 mm ns^{-1}, which is similar to the streamer propagation velocity obtained from the experiment (0.12 mm ns^{-1}). Similar to the experiment, the streamer propagation velocity increases after the streamer head reaches the middle part of the column (experimental result: 0.47 mm ns^{-1}, simulation result: 0.52 mm ns^{-1}).

Once the streamer head reaches the bottom of the column at $t_{sim} = 518$ ns, the maximum $N_2(C^3\Pi_u)$ and electron densities reappear at the top of the column. The concentration of $N_2(C^3\Pi_u)$ is mainly located in the upper half of the column and gradually decays until $t_{sim} = 600$ ns. After $t_{sim} = 600$ ns, the density of $N_2(C^3\Pi_u)$ and electron density on the dielectric column surface increases, indicating an increase in the discharge intensity along the dielectric column surface. As shown in figure S2, the discharge along the surface of the dielectric column expands. The growing process lasts until $t_{sim} = 720$ ns when the current reaches the second peak, after which the $N_2(C^3\Pi_u)$ and electron densities drop slowly. The $N_2(C^3\Pi_u)$ distribution in the simulation and the ICCD photo in the experiment indicate that the calculated discharge morphology is similar to the ICCD images during the rising edge of the pulse. Initially, a polar discharge occurs at the contact areas between different materials, which then evolves into a streamer discharge along the surface of the dielectric column. The discharge further expands on the surface of the dielectric column before gradually dissipating. Based on the similarity in discharge current and kinetics between the model and experiment, the model can assist to some extent in investigating the parameters associated with plasma catalysis that are unobtainable through experimentation. For instance, the model can provide insights into the electric field distribution on the catalytic surface in the section 3.2.

Reverse current peaks occur during the pulse falling edge in both experiment and simulation, indicating the occurrence

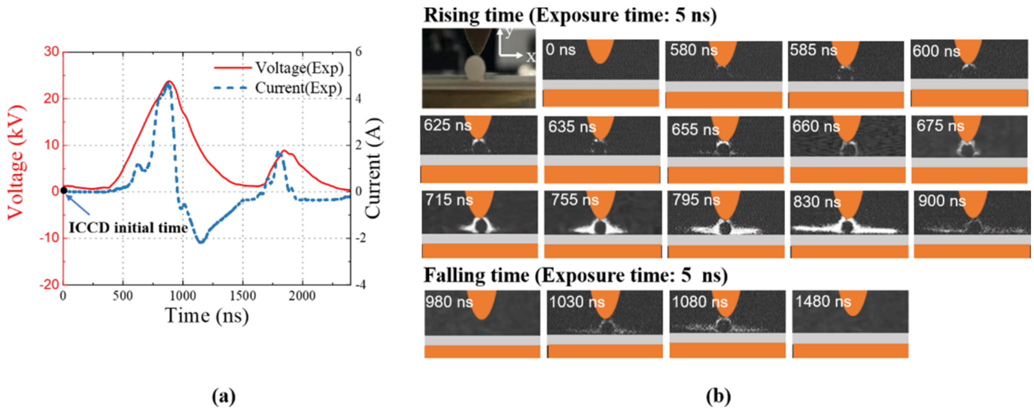

Figure 3. Discharge evolution of the PBR filled with the single Al_2O_3 column when the pulse peak is 24 kV (Electrodes: orange region; dielectric plate: light grey region. The time marked in each photo corresponds to the time in figure 3(a)).

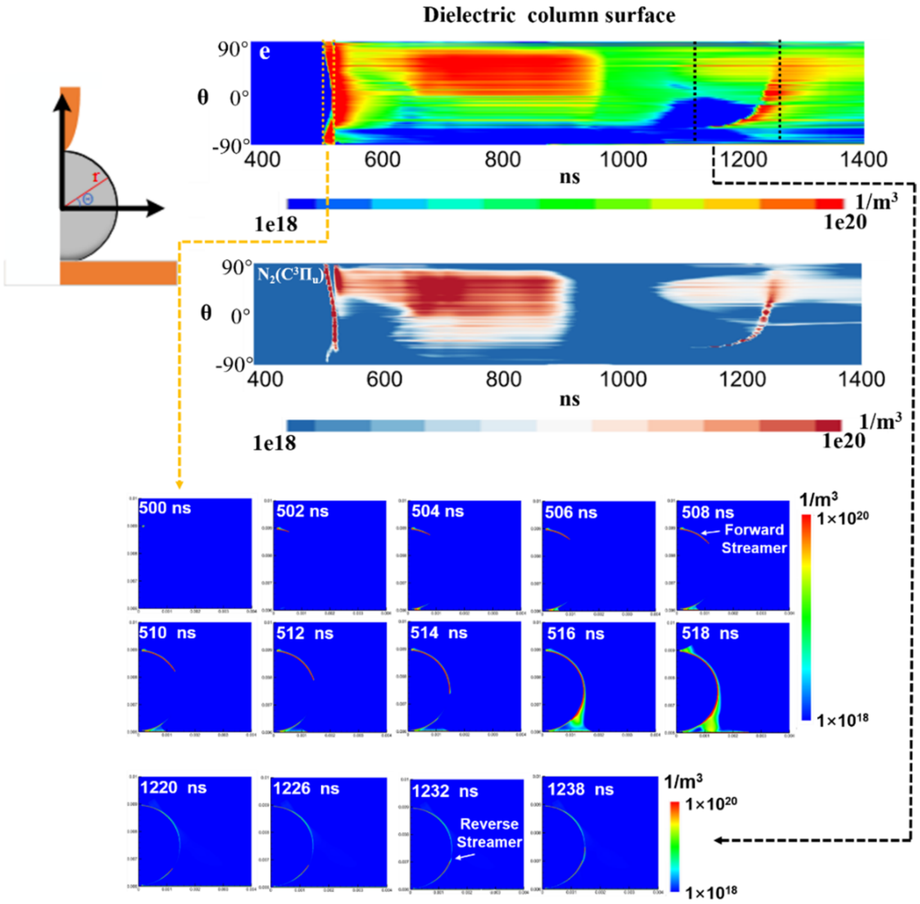

Figure 4. Simulated electron number density and $N_2(C^3\Pi_u)$ number density along the dielectric column surface.

of reverse breakdown. Unfortunately, the detailed discharge development process of PBR during reverse breakdown was not captured in our experiment due to the limitations of our ICCD camera. It can be seen from figure 4 that the maximum electron density and $N_2(C^3\Pi_u)$ density are observed at the bottom of the column at about $t_{sim} = 1180$ ns. The electron and $N_2(C^3\Pi_u)$ density increase upward along the dielectric column surface. The time-varying trend of electron density and $N_2(C^3\Pi_u)$ density at the bottom of the column corresponds to the development of the reverse streamer, as illustrated in figures 4 and S3.

3.2. The electric field distribution in PBR

In this section, we utilized EFISH to measure the electric field in proximity to the surface of the dielectric column and compared the measured results with simulation. The spatial distribution of the temporal electric field was obtained by changing

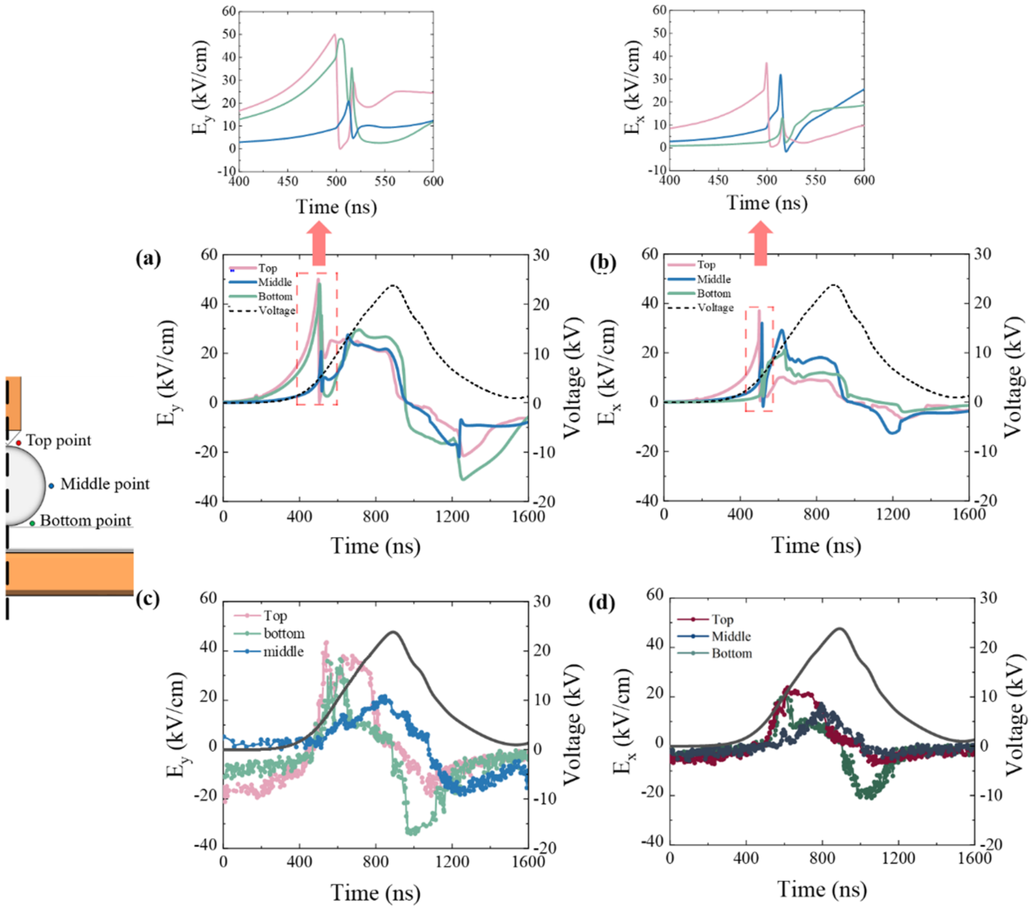

Figure 5. (a) Simulated E_y at different measurement locations. (b) Simulated E_x at different measurement locations. (c) Measured E_y at different measurement locations. (d) Measured E_x at different measurement locations.

the laser location. We conducted electric field measurements at three different locations: (i) the top measurement location near the top contact area; (ii) the middle measurement location near the middle part of the dielectric column; (iii) the bottom measurement location near the bottom contact area. The distribution of the measurement locations is illustrated in figure 5. The simulated electric field was obtained at the same locations as in the experiment. The EFISH calibration was done by using the parallel-plate electrode with a length of 30 mm and a discharge gap of 2 mm under the known electric field. It should be noted that only absolute electric field values can be obtained with EFISH. We analyzed the direction of the electric field according to the discharge current and discharge evolution. In our paper, we defined the vertical downward and horizontal rightward directions as the positive directions of the vertical electric field E_y and the horizontal electric field E_x.

As for E_{exp}, it can be seen from figures 5(c) and (d) that E_{exp} increases with the pulse. At around $t_{exp} = 580$ ns, the partial discharge appears at the top of the column, and $E_{exp(top)}$ (40 kV cm^{-1}) reaches its first peak. $E_{exp(top)}$ reaches another peak when the streamer head arrives at the top measurement location. When the surface streamer head arrives at the middle of the column, the $E_{exp(middle)}$ reaches its peak. As the pulse continues to rise, $E_{exp(middle)}$ rises again, reaching another maximum, before gradually dropping to zero. $E_{exp(bottom)}$ shows its first peak when a local discharge occurs at the bottom contact areas. A surface ionization wave is generated from the bottom contact areas and propagates along the surface of the dielectric plate. As a result, $E_{exp(bottom)}$ reaches another peak before dropping sharply. During the pulse falling time, the E_{exp} increases again and reaches its peak in reverse.

The simulated electric field E_{sim}, similar to the E_{exp}, exhibits its peaks with different polarities, as illustrated in figures 5(a) and (b). It can be seen from figures 5(a) and (b) that E_{sim} initially increases with the pulse. The simulated electric field at the top and middle of the column $E_{sim(top)}$ and $E_{sim(middle)}$ reaches peaks ($E_{ysim(top)} = 50.5$ kV; $E_{ysim(middle)} = 21.2$ kV) when the forward streamer head reaches the corresponding position. Subsequently, $E_{sim(top)}$ and $E_{sim(middle)}$ decrease rapidly due to the plasma shielding and the charge separation. As for $E_{sim(bottom)}$, a local discharge occurs at the bottom of the column during the propagation of the forward streamer. It causes the first peak of $E_{sim(bottom)}$ and the $E_{sim(bottom)}$ reaches another field peak when the streamer head arrives at the bottom of the column, which can be seen from the partially enlarged drawing of figures 5(a) and (b). The pulse is still rising, causing E_{sim} to increase again. The discharge along the column

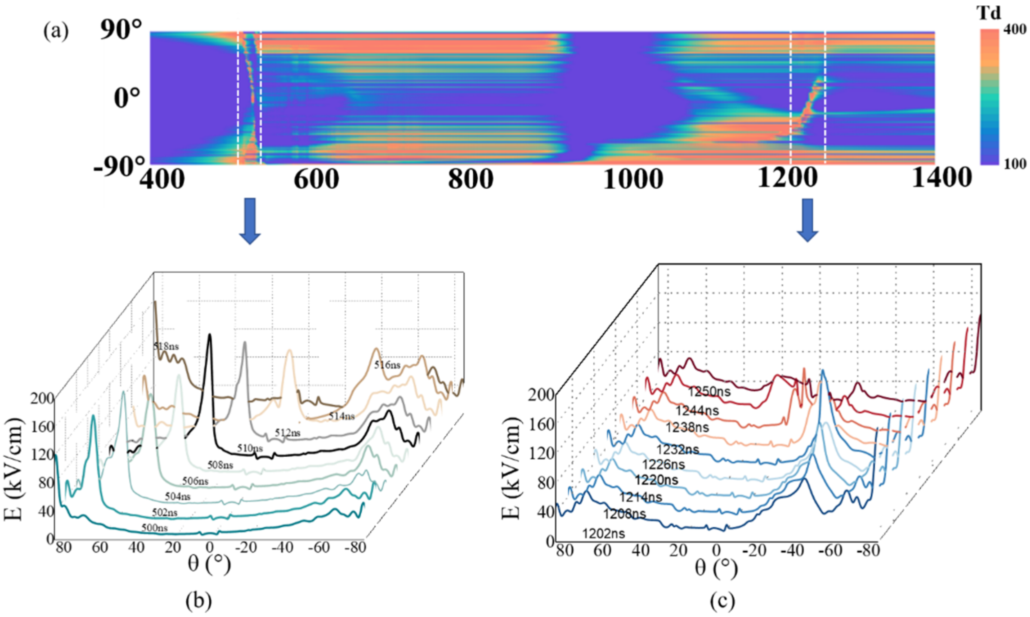

Figure 6. (a) Simulated electric field distribution on the surface of the dielectric column. (b) Simulated electric field evolution on the surface of the dielectric column during the propagation of the forward streamer. (c) Simulated electric field evolution on the surface of the dielectric column during the propagation of the forward streamer.

expands during the growth process of E_{sim}. E_{sim} reaches a maximum value and then decays to zero slowly. During the pulse falling edge, E_{sim} grows in reverse and reaches the reverse peak and then decays again.

However, there are still differences between E_{sim} and E_{exp}. Firstly, the most prominent difference between E_{exp} and E_{sim} is the presence of an offset electric field in E_{exp} prior to pulse. The discrepancy arises from the fact that the E_{exp} was obtained in the PBR powered by a nanosecond pulse at a pulse repetition rate of 1 Hz. In contrast, the simulation results were obtained during a single pulse. The offset field is generated due to the residual surface charges from the previous pulse. Moreover, E_{sim} and E_{exp} do not exhibit an exact time matching. This discrepancy can be attributed to two factors. On the one hand, the signal transmission time in cable and the response time of the SHG detector contribute to the time mismatching. On the other hand, E_{exp} exhibits an offset electric field prior to the main pulse. As the applied electric field increases, it has to counteract the influence of the offset electric field. As depicted in figures 5(c) and (d), E_{exp} gradually diminishes to zero and then increases reversely. Nonetheless, E_{sim} initially increases as the applied voltage increases. The discrepancy between E_{exp} and E_{sim} in offset electric field also contributes to the time mismatching between E_{exp} and E_{sim}. Secondly, the 2D model in our study indicates uniform discharge along the z-axis direction. However, the discharge observed in experiments is not completely uniform due to the slow pulse rising rate. To achieve uniform discharge across the millimeter-scale discharge gap in air, a pulse rising rate of at least 10 kV ns^{-1} is typically required. The disparity in discharge uniformity leads to a significantly higher peak value E_{sim} of the forward streamer. Since the temporal resolution of the EFISH measurement is limited by the laser pulse width (∼5 ns), the evolution of E_{exp} induced by discharge cannot be well captured. Thirdly, the distance between the laser beam and the surface of the packing material is constrained by the laser radius. Since a thin surface streamer propagates along the surface of the dielectric column, the laser beam cannot fully pass through the streamer channel, which results in the underestimate of the peak value of E_{exp}.

The measurement of surface electric field $E_{surface}$ by EFISH is challenging due to the significant background SHG generated when the laser reaches the dielectric surface. However, investigating the electric field distribution on the catalyst is crucial to comprehending the interaction between the plasma and the catalyst. In this section, we studied the electric field on the catalyst surface through the model. Figure 6(a) shows that during the pulse rising time, the enhancement of the $E_{surface}$ initially occurs at the top and bottom parts of the column, where the catalyst contacts other materials due to dielectric polarization. As the pulse voltage continues to increase, a forward surface streamer is generated when the self-sustaining discharge condition is reached. The evolution of the $E_{surface}$ during the propagation of the surface streamer is shown in figure 6(b). The $E_{surface}$ reaches a peak of 125 kV cm^{-1}–200 kV cm^{-1} when the surface streamer head arrives. The $E_{surface}$ drops after the streamer head passes due to the remaining space charges generated in the weakly ionized channel. It can also be seen in figure 6(b) that the streamer is accelerated after the streamer head reaches the middle part of the dielectric column at $t_{sim} = 514$ ns. After the streamer head arrives at the bottom of the column, the enhancement of the

$E_{surface}$ appears again at the top of the column. The $E_{surface}$ at the contact area is significantly higher than that in other areas during the rest of the pulse rising time. During the falling edge of the pulse, the $E_{surface}$ strengthens at both the top and bottom of the column as a reverse streamer is generated from the bottom of the column. Figure 6(c) represents the evolution of the $E_{surface}$ during the propagation of the reverse surface streamer, and the electric field at the reverse surface streamer head is lower than that at the forward surface streamer head.

4. Conclusion

In this paper, the discharge characteristics and electric field distribution in a simplified PBR under positive nanosecond pulses in ambient air were investigated through numerical simulations and experiments. The discharge process of PBR involves initial polar discharge at contact areas during pulse rising, followed by streamer discharge along the packing material surface. After the forward streamer, the discharge spreads on the dielectric column surface. During pulse falling, the reverse streamer propagates in the lower half of the column. The velocity of the forward streamer is higher than the velocity of the reverse streamer, as evidenced by both the experimental and simulation results.

The electric field distribution of the PBR is firstly measured by E-FISH. The results show that the spatiotemporal electric field has an offset field generated by the surface charge accumulated on the dielectric surface. The electric field reaches peaks with opposite polarity during the rising and falling edge of the pulse. During the pulse rising time, E_{exp} reached its peak when the streamer head arrived at the corresponding locations (i.e. $E_{ypeak\ (top)} = 37.8\ \mathrm{kV\ cm^{-1}}$, $E_{ypeak(middle)} = 14.1\ \mathrm{kV\ cm^{-1}}$, and $E_{ypeak(bottom)} = 36.6\ \mathrm{kV\ cm^{-1}}$). During the pulse falling time, E_{exp} grew reversely. The reverse E_{exp} peaks at the top and bottom parts of the column were slightly higher than that at the middle parts of the column (i.e. $E_{ypeak(top)} = -20.68\ \mathrm{kV\ cm^{-1}}$ $E_{ypeak(middle)} = -11.24\ \mathrm{kV\ cm^{-1}}$, and $E_{ypeak(bottom)} = -34.4\ \mathrm{kV\ cm^{-1}}$). By investigating the spatial distribution of the electric field, the advancement of the surface streamer can be reflected from the electric field measurement results.

Our findings present a similarity between the calculated and measured electric field results. The electric field distribution on the dielectric column surface was investigated through the simulation. During the propagation of the surface streamer, the electric field at different positions on the surface reaches the maximum with the arrival of the streamer head, and decays rapidly due to plasma shielding. At the rest of the time, strong electric fields appear at the contact parts. The magnitudes of electric fields in the forward streamers are larger than those of the reverse streamers. However, there are still discrepancies between the E_{exp} and E_{sim}. The most notable one is the presence of the offset electric field in E_{exp}. Besides, the time mismatching between E_{sim} and E_{exp} might be due to the signal delay in the experiment and the initially biased electric field in E_{exp}.

In the future, the effects of different factors on the plasma characteristics of PBR will be investigated to reveal the coupling mechanism of plasma catalysis.

Data availability statement

All data that support the findings of this study are included within the article (and any supplementary files).

Acknowledgments

This work was supported by National Nature Science Foundation of China (51977063), and Natural Science Foundation of Hunan Province—Outstanding Youth Project (2022JJ20010), open project (SKLD21KZ06) from State Key Laboratory of Power System and Generation Equipment, research project of the Hunan Provincial Department of Education (21B0019).

ORCID iDs

She Chen https://orcid.org/0000-0001-7013-1442
Yifei Zhu https://orcid.org/0000-0001-8989-0051
Chijie Zhuang https://orcid.org/0000-0002-2579-050X

References

[1] Harling A M, Demidyuk V, Fischer S J and Whitehead J C 2008 Plasma-catalysis destruction of aromatics for environmental clean-up: effect of temperature and configuration *Appl. Catal.* B **82** 180
[2] Kim H H, Teramoto Y, Ogata A, Takagi H and Nanba T 2016 Plasma catalysis for environmental treatment and energy applications *Plasma Chem. Plasma Process.* **36** 45
[3] Ju Y and Sun W 2015 Plasma assisted combustion: dynamics and chemistry *Prog. Energy Combust. Sci.* **48** 21
[4] Carreon M L 2019 Plasma catalytic ammonia synthesis: state of the art and future directions *J. Phys. Appl. Phys.* **52** 483001
[5] Chen L, Zhang X, Huang L and Lei L 2010 Application of in-plasma catalysis and post-plasma catalysis for methane partial oxidation to methanol over a Fe_2O_3-CuO/γ-Al_2O_3 catalyst *J. Nat. Gas Chem.* **19** 628
[6] Pylinina A I and Mikhalenko I I 2013 Activation of Cu-, Ag-, Au/ZrO2 catalysts for dehydrogenation of alcohols by low-temperature oxygen and hydrogen plasma *Theor. Exp. Chem.* **49** 65–69
[7] Demidyuk V and Whitehead J C 2007 Influence of temperature on gas-phase toluene decomposition in plasma-catalytic system *Plasma Chem. Plasma Process.* **27** 85
[8] Tu X, Whitehead J C and Nozaki T Eds. 2019 *Plasma Catalysis: Fundamentals and Applications* (*Springer Series on Atomic, Optical, and Plasma Physics*) (Cham: Springer International Publishing) (https://doi.org/10.1007/978-3-030-05189-1)
[9] Rousseau A, Guaitella O, Ropcke J, Gatilova L V and Tolmachev Y A 2004 Combination of a pulsed microwave plasma with a catalyst for acetylene oxidation *Appl. Phys. Lett.* **85** 2199
[10] Chang J S, Kostov K G, Urashima K, Yamamoto T, Okayasu Y, Kato T, Iwaizumi T and Yoshimura K 2000 Removal of NF3 from semiconductor-process flue gases by

tandem packed-bed plasma and adsorbent hybrid systems *IEEE Trans. Ind. Appl.* **36** 1251
[11] Li Y, Yang D, Qiao J, Zhang L, Wang W, Zhao Z, Zhou X, Yuan H and Wang W-C 2020 The dynamic evolution and interaction with dielectric material of the discharge in packed bed reactor *Plasma Sources Sci. Technol.* **29** 055004
[12] Li Y, Yang D, Qiao J, Zhang L, Wang W, Zhao Z, Zhou X, Yuan H and Wang W-C 2021 Discharge modes and characteristics optimization of nanosecond pulsed discharge in packed bed reactor *J. Phys. Appl. Phys.* **54** 245206
[13] Kang W S, Kim H H, Teramoto Y, Ogata A, Lee J Y, Kim D W, Hur M and Song Y H 2018 Surface streamer propagations on an alumina bead: experimental observation and numerical modeling *Plasma Sources Sci. Technol.* **27** 015018
[14] Kim H H and Ogata A 2011 Nonthermal plasma activates catalyst: from current understanding and future prospects *Eur. Phys. J. Appl. Phys.* **55** 13806
[15] Kim -H-H, Teramoto Y, Sano T, Negishi N and Ogata A 2015 Effects of Si/Al ratio on the interaction of nonthermal plasma and Ag/HY catalysts *Appl. Catal.* B **166–167** 9–17
[16] Kim H-H, Kim J-H and Ogata A 2009 Microscopic observation of discharge plasma on the surface of zeolites supported metal nanoparticles *J. Phys. D: Appl. Phys.* **42** 135210
[17] Mujahid Z-I and Hala A 2018 Plasma dynamics in a packed bed dielectric barrier discharge (DBD) operated in helium *J. Phys. Appl. Phys.* **51** 11LT02
[18] Wang W, Kim H-H, Van Laer K and Bogaerts A 2018 Streamer propagation in a packed bed plasma reactor for plasma catalysis applications *Chem. Eng. J.* **334** 2467
[19] Zhang Q and Bogaerts A 2018 Propagation of a plasma streamer in catalyst pores *Plasma Sources Sci. Technol.* **27** 035009
[20] Van Laer K and Bogaerts A 2017 How bead size and dielectric constant affect the plasma behaviour in a packed bed plasma reactor: a modelling study *Plasma Sources Sci. Technol.* **26** 85007
[21] Kruszelnicki J, Engeling K W and Foster J E 2017 Propagation of negative electrical discharges through 2-dimensional packed bed reactors *J. Phys. D: Appl. Phys.* **50** 25203
[22] Wang W, Butterworth T and Bogaerts A 2021 Plasma propagation in a single bead DBD reactor at different dielectric constants: insights from fluid modelling *J. Phys. Appl. Phys.* **54** 214004
[23] Van Laer K and Bogaerts A 2017 Influence of gap size and dielectric constant of the packing material on the plasma behaviour in a packed bed DBD reactor: a fluid modelling study: influence of gap size and dielectric constant *Plasma Process. Polym.* **14** 1600129
[24] Xiong R, Zhao P, Wang H, Zhang Y and Jiang W 2020 Impact of different packing beads methods for streamer generation and propagation in packed-bed dielectric barrier discharge *J. Phys. Appl. Phys.* **53** 185202
[25] Wan M, Yue H, Notarangelo J, Liu H and Che F 2022 Deep learning-assisted investigation of electric field—dipole effects on catalytic ammonia synthesis *JACS Au* **2** 1338–49
[26] Dogariu A, Goldberg B M, O'Byrne S and Miles R 2017 Species-independent femtosecond localized electric field measurement *Phys. Rev. Appl.* **7** 024024
[27] Goldberg B M, Chng T L, Dogariu A and Miles R B 2018 Electric field measurements in a near atmospheric pressure nanosecond pulse discharge with picosecond electric field induced second harmonic generation *Appl. Phys. Lett.* **112** 064102
[28] Goldberg B M, Reuter S, Dogariu A and Miles R 2019 1D time evolving electric field profile measurements with sub-ns resolution using the E-FISH method *Opt. Lett.* **44** 3853
[29] Cui Y, Zhuang C and Zeng R 2019 Electric field measurements under DC corona discharges in ambient air by electric field induced second harmonic generation *Appl. Phys. Lett.* **115** 244101
[30] Cui Y, Wang H, Zhuang C, Luo H, Wang X and Zeng R 2020 Electric field measurement in dielectric barrier discharges using electric field induced second harmonic generation in ambient air *IEEE Trans. Dielectr. Electr. Insul.* **27** 2071
[31] Huang B, Zhang C, Adamovich I, Akishev Y and Shao T 2020 Surface ionization wave propagation in the nanosecond pulsed surface dielectric barrier discharge: the influence of dielectric material and pulse repetition rate *Plasma Sources Sci. Technol.* **29** 044001
[32] Chng T L, Starikovskaia S M and Schanne-Klein M 2020 Electric field measurements in plasmas: how focusing strongly distorts the E-FISH signal *Plasma Sources Sci. Technol.* **29** 125002
[33] Nakamura S, Sato M, Fujii T, Kumada A and Oishi Y 2021 Electric-field-profile measurement along a probing laser path based on electric-field-induced second-harmonic generation *Phys. Rev.* A **104** 053511
[34] Zhu Y, Chen X, Wu Y and Starikovskaia S 2021 PASSKEy code [software] (Paris: Science and Technology of Plasma Dynamics Laboratory, Xi'an, China and laboratoire de physique des plasmas) (available at: www.plasma-tech.net/parser/passkey/)
[35] Zhu Y, Shcherbanev S, Baron B and Starikovskaia S 2017 Nanosecond surface dielectric barrier discharge in atmospheric pressure air: i. measurements and 2D modeling of morphology, propagation and hydrodynamic perturbations *Plasma Sources Sci. Technol.* **26** 125004
[36] Chen X, Zhu Y, Wu Y, Su Z and Liang H 2020 Modeling and theoretical analysis of SDBD plasma actuators driven by fast-rise–slow-decay pulsed-DC voltages *J. Phys. Appl. Phys.* **53** 465202
[37] Ma X, Zhu Y, Wu Y, Chen X and Lin B 2021 Multi-physics modeling of a spark plasma jet igniter *J. Phys. Appl. Phys.* **55** 035201
[38] Zhu Y and Starikovskaia S 2018 Fast gas heating of nanosecond pulsed surface dielectric barrier discharge: spatial distribution and fractional contribution from kinetics *Plasma Sources Sci. Technol.* **27** 124007
[39] Zhu Y, Chen X, Wu Y, Hao J, Ma X, Lu P and Tardiveau P 2021 Simulation of ionization-wave discharges: a direct comparison between the fluid model and E-FISH measurements *Plasma Sources Sci. Technol.* **30** 075025
[40] Ren C, Huang B, Qiu J, Zhang C, Qi B, Chen W and Shao T 2022 Is an extended barrier-free discharge under nanosecond-pulse excitation really diffuse? *J. Phys. Appl. Phys.* **55** 235204